Photo-organometallic, Nanoparticle Nucleation on Graphene for Cascaded Doping

Songwei Che, Sanjay K. Behura, and Vikas Berry*

Department of Chemical Engineering, University of Illinois at Chicago, 945 W. Taylor Street, Chicago, Illinois 60607, United States

S *Supporting Information*

ABSTRACT: Controlling the doping levels in graphene by modifying the electric potential of interfaced nanostructures is important to understand "cascaded-doping"-based applications of graphene. However, graphene does not have active sites for nanoparticle attachment, and covalently adding functional groups on graphene disrupts its planar sp^2-hybridization, affecting its cascaded doping. Here we show a hexahepto (η^6) photo-organometallic chemistry to interface nanoparticles on graphene while retaining the sp^2-hybridized state of carbon atoms. For testing cascaded doping with ethanol interaction, transition metal oxide nanoparticles (TMONs) (Cr_2O_3/CrO_3, MoO_3, and WO_3) are attached on graphene. Here, the transition metal forms six σ-bonds and π-back-bonds with the benzenoid rings of graphene, while its opposite face binds to three carbonyl groups, which enable nucleation and growth of TMONs. With a radius size ranging from 50 to 100 nm, the TMONs downshift the Fermi level of graphene (-250 mV; p-doping) *via* interfacial charge transfer. This is consistent with the blue shift of graphene's G and 2D Raman modes with a hole density of 3.78×10^{12} cm^{-2}. With susceptibility to ethanol, Cr_xO_3 nanoparticles on graphene enable cascaded doping from ethanol that adsorbs on Cr_xO_3, leading to doping of graphene to increase the electrical resistance of the TMONs−graphene hybrid. This nanoparticle-on-graphene construct can have several applications in gas/vapor sensing, electrochemical catalysis, and high-energy-density supercapacitors.

KEYWORDS: *graphene, surface functionalization, cascaded doping, metal oxide nanoparticles, photochemistry*
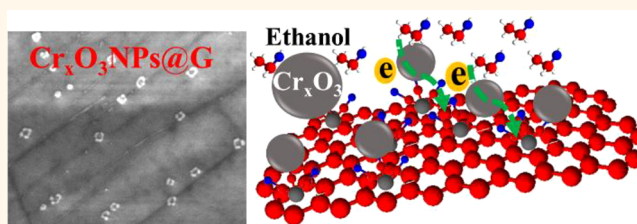
With a unique linear electronic band dispersion and massless Dirac fermions, graphene, a two-dimensional (2D) monolayer of sp^2 carbon atoms with hexagonal crystal structure, is an excellent platform for studying fundamental physics and for advanced applications. Further, graphene's large surface area (2600 m²/g), high transparency (97.7%), flexibility, and superior electrical (10^8 S/m) and thermal (2600−5300 W/mK) conductivities make it a promising candidate for optoelectronics,[1,2] nanoelectronics,[3] electrochemical energy storage[2] (batteries and capacitors), and sensors.[4,5] Low-dimensional transition metal oxides (WO_3, Fe_2O_3, MnO_x, NiO, and CoO_x) are an important class of nanostructures that exhibit extensive applications that leverage several properties including structural,[6,7] magnetic,[8] optical,[9] and chemiresistive.[10] For example, tungsten trioxide (WO_3) is sensitive and selective to the detection of various gases (NO_x,[11,12] O_3,[13] H_2S[14]) and vapors.[15,16] Molybdenum trioxide's (MoO_3's) high chemical stability, high lithium storage capacity, and high specific capacity make it a promising electrode material for lithium ion batteries.[17−19] MoO_3 nanoparticle's (NP) strong affinity to hydrogen sulfide (H_2S) enables its composite with reduced graphene oxide (rGO) to exhibit high selectivity to H_2S among other analytes including ethanol, carbon monoxide, and nitric oxide.[20] Chromium oxide has different oxidation states (CrO_3, Cr_2O_3, CrO_2) and its

magnetic properties vary with different crystallography, stoichiometry, and nanoparticle size.[21−23] In this work, we combine the unique properties of TMONs with graphene in a hybrid composite system without disrupting graphene's lattice planarity.

However, pristine graphene has no molecular sites for efficient attachment of nucleating particles. Most chemistries to interface transition metal oxide nanoparticles (TMONs) on graphene employ graphene oxide (GO) and rGO, in which the oxy-groups (*e.g.*, carboxyl, hydroxyl, epoxy)[24] on GO and rGO offer active sites for attachments of NPs. These covalent-functionalized forms of graphene convert sp^2-hybridized carbon atoms to sp^3 hybridization, resulting in orders of magnitude loss in charge carrier mobility, thus limiting their applications in sensing, electrochemical catalysis, and nano-electronics. The main techniques to synthesize graphene−TMONs nanocomposites include solvothermal and hydrothermal methods. In such a process, high temperature (120−200 °C) and high pressure are used to grow TMONs on graphene nanomaterials (nanosheets or nanoplates) by adding toxic reducing reactants (*e.g.*, ethylene glycol, hydrazine.).[25−29]
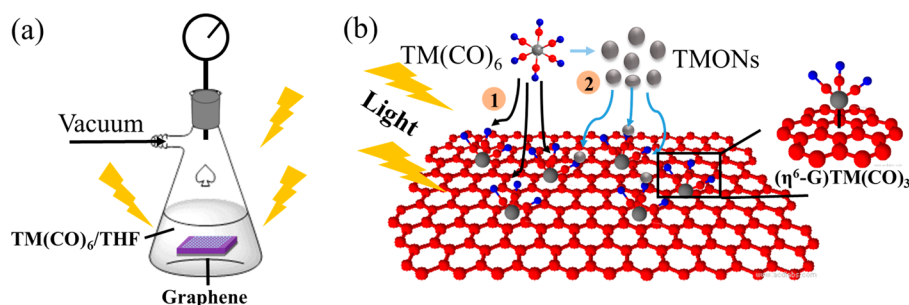
Figure 1. Experimental setup and chemical mechanism: (a) Solution-process steps for the photo-organometallic reaction on CVD graphene and (b) pathways of transition metal oxide nanoparticle deposition on the graphene surface *via* a photochemical strategy. The right inset is η^6-functionalized graphene after binding transition metal tricarbonyls ($TM(CO)_3$). Processes 1 and 2 are represented in eqs 1 and 2. TM represents transition metal, including chromium, molybdenum, and tungsten.

Nevertheless, in chemically functionalized graphene, some organometallic chemistries can modify graphene with negligible change in graphene's crystallographic planarity.[30] In the η^6-functionalized graphene, transition metal (*e.g.*, chromium) tricarbonyl moieties coordinately bind to six carbon atoms of the benzenoid rings on graphene. Sarkar and co-workers[31,32] have synthesized high-mobility hexahapto-functionalized graphene under refluxing conditions (40−140 °C, 6−48 h) using variable chromium carbonyl complexes. Moreover, a vapor-phase route has been developed to form a (η^6-graphene)Cr-$(CO)_3$ complex by dissociating $Cr(CO)_6$ inside a tube furnace (130 °C, 40 min).[33] Also, a photochemical method could effectively organometallic-functionalize carbon materials (*e.g.*, single-walled carbon nanotubes).[34] Three-dimensional cross-linked graphene nanoplatelets (GNPs) are synthesized under irradiation of UV light in which bis-hexahapto bonds work as bridges to interconnect GNPs and electrical conductivity is enhanced correspondingly.[35] The same photoactivated reactions are also performed on single-layer graphene to synthesize a (η^6-graphene)CrL [L = C_6H_6, $(CO)_3$] complex, leading to enhanced conductivity.[36] In such a method, UVC light (wavelength λ = 254 nm) is employed to provide dissociation energy of metal−CO bonds to further form (η^6-graphene)Cr-$(CO)_3$ in very short times (10−110 s). However, interfacing TMONs on monolayer graphene *via* a one-step, photo-chemical and organometallic route has not been shown, which is performed under mild conditions (low temperature, low vacuum), avoiding toxic reducing chemicals.

In this work, TMONs are incorporated on large-scale monolayer graphene produced by chemical vapor deposition (CVD) by a one-step, photo-organometallic route. By combination of thermal (temperature) and light energy (LED white light, wavelength λ = 450−475 nm), η^6-functionalized graphene is synthesized. Simultaneously TMONs are formed, nucleated, and attached on such hexahapto-modified graphene. Raman spectroscopy is used to characterize the TMONs−graphene composite, showing slight enhancement (less than 10%) in the intensity of the D-peak with a blue shift in both G- and 2D-bands. *Via* field emission scanning electron microscopy (FESEM), chromium oxide nanoparticles (Cr_xO_3, consisting of CrO_3 and Cr_2O_3), molybdenum oxide (MoO_3), and tungsten oxide (WO_3) nanoparticles with different shapes and sizes are observed on the graphene surface, respectively. Moreover, variable valence phases formed in TMONs are studied by X-ray photoelectron spectroscopy (XPS). Further, the electronic transport measurements on back-gated graphene transistors suggest that the

electrical conductivity is enhanced, while the mobility is reduced as the Fermi level is lowered by 250 mV postattachment of Cr_xO_3 nanoparticles. In the ethanol sensing test, the resistance of Cr_xO_3 NPs incorporated graphene is increased, resulting from the absorption of ethanol gas. A cascaded-doping mechanism is proposed to explain the enhanced resistance when Cr_xO_3 NPs incorporated graphene interfaces with ethanol. This represents that electrons transfer from ethanol to Cr_xO_3 NPs, followed by the transport of electrons from Cr_xO_3 NPs to graphene.

The Chemical Mechanism. The photochemistry developed here to bind TMONs on graphene involves two simultaneous processes, as shown in Figure 1. First, graphene is chemically functionalized with $TM(CO)_6$ *via* the η^6-chemistry[33] to form (η^6-graphene)$TM(CO)_3$, providing molecular anchors for NP nucleation and growth. Second, by absorbing energy from high-energy UV or visible photons, the $TM(CO)_6$ molecules dissociate into TM radicals that react with dissolved O_2 to form transition metal oxide radicals and NPs. The radicals nucleate and grow, and the NPs deposit on the (η^6-graphene)$TM(CO)_3$ sites on graphene.

For the η^6 reaction, it is known that the C≡O groups from the metal carbonyl complexes can be substituted by other ligands, such as tetrahydrofuran (THF).[37] It is also reported that a mild photochemical route can synthesize arene tricarbonyl chromium(0) at room temperature with a medium-pressure mercury lamp.[38] In our process, three C≡O groups from $TM(CO)_6$ are dissociated under irradiation to form $TM(CO)_3$ groups that graft on the benzenoid rings of graphene with carbon monoxide as a byproduct, as shown in the following reaction (eq 1). As shown in Figure 1b, right inset, $TM(CO)_3$ moieties bind with six carbon atoms of benzenoid rings on graphene *via* coordination bonds. The metal atoms are located on the top center of the benzenoid rings, while on the other side of the metal atoms carbon and oxygen atoms from carbonyl groups are parallel with the graphene sheets. To some extent, the interaction of graphene to $Cr(CO)_3$ moieties is similar to that in (η^6-arene)$Cr(CO)_3$, in which the carbon atoms from the benzene ring are located at the same distance from chromium atoms with the same angle between carbon atoms (120 ± 0.01°).[39,40] Also, a DFT simulation on organometallic hexahepto-functionalized graphene confirms that in (η^6-graphene)$Cr(CO)_3$ the bonding lengths between carbon atoms of graphene's benzenoid ring and Cr are almost the same at 2.247 Å.[30] This indicates that the graphene's sp^2 hybrid state and planarity are preserved after η^6 chemistry.
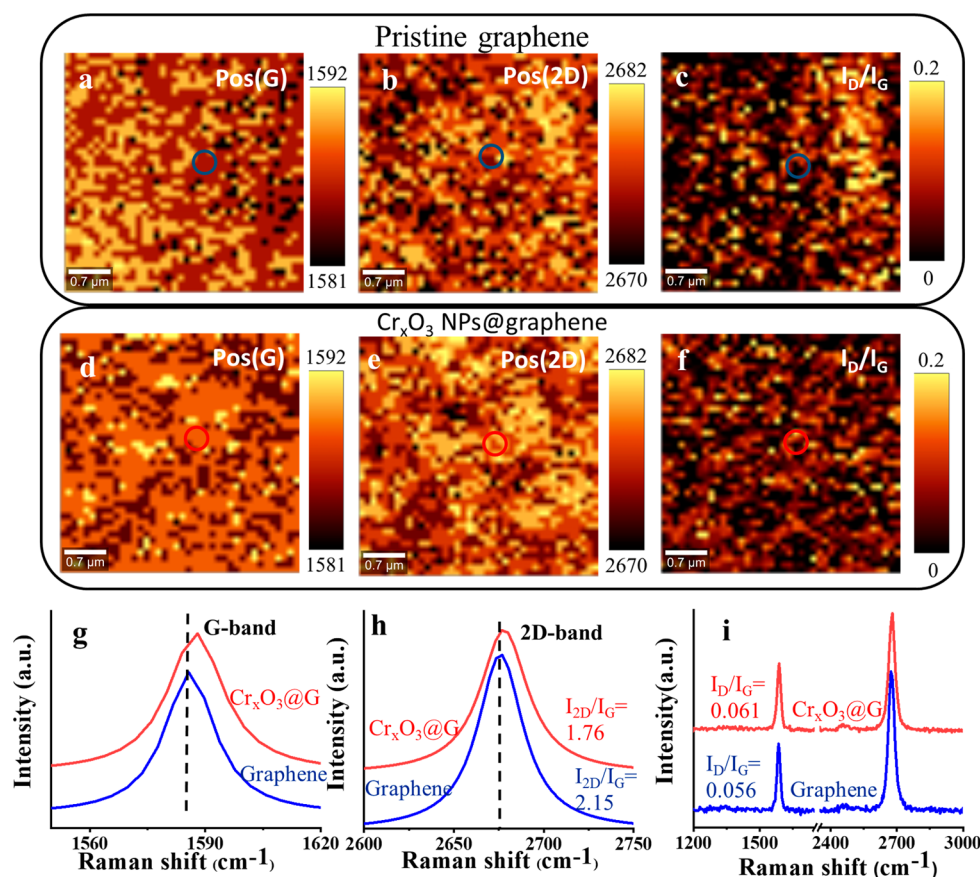
Figure 2. Raman spectroscopic characterization of pristine graphene and Cr_xO_3 nanoparticles decorated graphene: (a, d) Scanning Raman mappings of the G-band position (ranging from 1581 to 1592 cm^{-1}) before (a) and after (d) the attachment of Cr_xO_3 NPs; (b, e) 2D-band position (ranging from 2670 to 2682 cm^{-1}) before (b) and after (e) the attachment of Cr_xO_3 NPs; (c, f) Raman images of D-to-G peak intensity ratio (I_D/I_G) of graphene (c) and after (f) incorporation of Cr_xO_3 NPs. (g) G-band Raman spectra of pristine graphene (blue line) and graphene with attachment of Cr_xO_3 NPs (red line); (h) Raman peak shift of the 2D band before (blue line) and after the incorporation of Cr_xO_3 NPs on graphene (red line); (i) Raman spectra of graphene and Cr_xO_3 NPs decorated graphene by averaging the circled area in the Raman maps.

$$TM(CO)_6 + graphene$$
$$\Rightarrow (\eta^6\text{-graphene})TM(CO)_3 + 3CO \qquad (1)$$
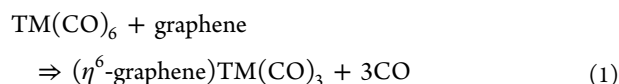
For the second process, the absorbed photons break the bonding between transition metals and carbonyls (TM−CO). Then the photodissociated transition metal radicals react with O_2 to form TMONs, as represented in the chemical reaction shown in eq 2.

$$2TM(CO)_6 + O_2 \Rightarrow 2TMONs + 12CO \qquad (2)$$

The key source of oxygen is the small volume of water dissolved in nondehydrated THF.[41] Due to its high photoactivity, transition metal carbonyl complexes (*e.g.*, $Fe_2(CO)_9$,[42] $Ni(CO)_4$, $Mo(CO)_6$[43]) are widely used as precursors to synthesize metal nanoparticles *via* the photolysis route. For example, Mo nanoparticles are prepared using Kr−F laser (wavelength: 248 nm) pulse photolysis of $Mo(CO)_6$ vapor mixed with argon. At room temperature, the mean diameters of Mo nanoparticles are variable in the range of 3−13 nm, depending on the numbers of excimer Kr−F laser pulses.[44]

Further, it is observed that a large quantity of MoO_3 nanoparticles are attached on the graphene surface (Figure S2) compared with pristine graphene (Figure S3), while very few nanoparticles are found on silicon dioxide-coated Si

(SiO_2/Si) (possibly on defect sites). This confirms that the η^6-binding sites on graphene are essential for the nucleation/growth and incorporation of TMONs.

RESULTS AND DISCUSSION

Confocal Raman vibrational spectroscopy is a versatile tool to investigate the surface doping effect in graphene.[45,46] Figure 2a and b show the G-band (from 1581 to 1592 cm^{-1}) and 2D-band (from 2670 to 2682 cm^{-1}) position mapping of pristine graphene on a SiO_2/Si chip obtained by scanning a region of 4 × 4 μm^2 graphene before and after TMONs attachment using 532 nm laser excitation (confocal scanning Raman spectrometer). The ratio of the D-peak intensity to G-peak intensity (I_D/I_G) is used to quantify the defects in graphene.[47] Figure 2c shows a low I_D/I_G (~0.056), indicating that a high-quality graphene with negligible defects[48] is used for nanoparticle anchoring. The Raman spectra in Figure 2g−i are achieved by averaging the circular area. After the attachment of Cr_xO_3 NPs on graphene by the photochemical strategy (where x = 1 or 2, based on the XPS data), there is a blue shift in both G-band (~3 cm^{-1}) and 2D-band (~2 cm^{-1}) positions (Figure 2). The Raman shift suggests that the deposition of Cr_xO_3 NPs leads to p-doping (hole doping)[49] of graphene. Also, the p-doping of graphene reduces the intensity of the 2D peak (I_{2D}/I_G) by 18%. It is reported in the literature[50] that the functional group
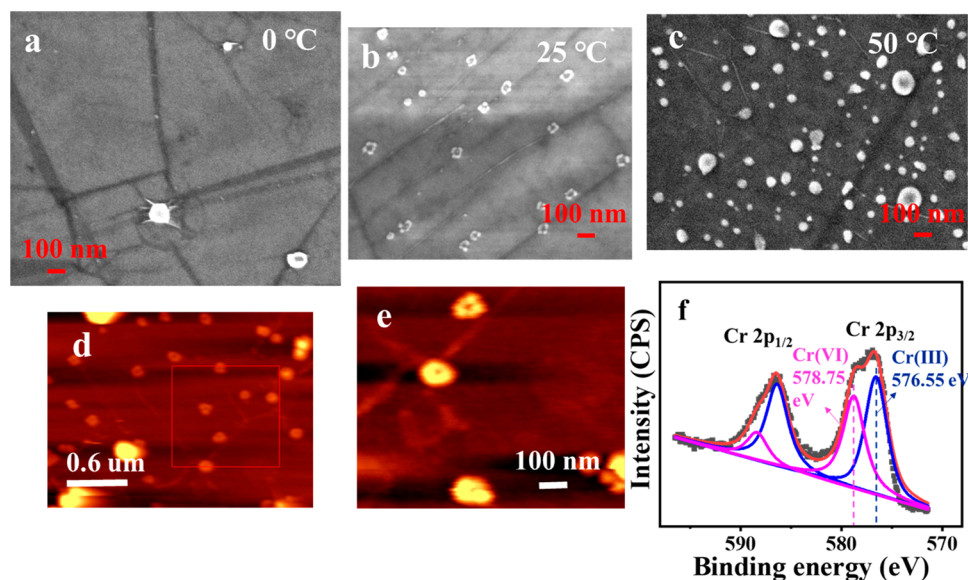
Figure 3. FESEM and XPS characterization of Cr_xO_3NPs-decorated graphene: (a−c) FESEM images of graphene with the attachment of Cr_xO_3 NPs at 0 °C (a), 25 °C (b), and 50 °C (c). (d and e) AFM images of bracelet-shape Cr_xO_3 NPs incorporated on graphene and (e) obtained by scanning the square-region in (d). (f) High-resolution XPS spectra of Cr 2p-peaks.

$Cr(CO)_3$ in η^6 chemistry is electron-withdrawing (the electrons transfer from graphene to $Cr(CO)_3$), which corresponds to the hole-doping in graphene. Moreover, the transition metal oxide has a high work function ($\Phi_{TMO} > 5$ eV),[51] while that of graphene (Φ_G) is 4.48 eV.[52] Since $\Phi_{TMO} > \Phi_G$, the Fermi level shifts downward by moving electrons to TMONs from graphene,[53,54] which is consistent with the results of electrical measurements shown later. Further, the I_D/I_G intensity ratio becomes 0.061 after the attachments of Cr_xO_3 nanoparticles ($I_D/I_G \approx 0.056$, before attachment) (Figure 1c, f, and i), indicating that the attachment of TMONs on the graphene surface does not disrupt graphene's trigonal-planar sp^2 lattice structure. This result corroborates the non-destructive η^6 chemistry.[33] The attachment of Cr_xO_3 NPs on graphene is sensitive to the process temperature, as observed in the FESEM images (Figure 3a−c). The density of NPs increased with process temperature (0 to 50 °C), which is attributed to the η^6 chemistry and NP formation being endothermic. Sarkar and co-workers[31] have functionalized single-layer graphene by using chromium hexacarbonyl (Cr-$(CO)_6$) as reactant in refluxing conditions (140 °C). Also, a vapor-phase η^6-functionalization of graphene has been achieved at 130 °C under low vacuum.[33] Moreover, Cr, Mo, W, and other transition metal nanoparticles (Fe, Ru, Os) have been stably synthesized in ionic liquids by thermal decomposition (90−250 °C, 6−12 h) and photolysis (UV, 15 min), in which the mono-, di-, and trinuclear metal carbonyl precursors are completely decomposed by absorbing the supplied thermal and photonic energy.[42,43] It is also suggested that a faster decomposition and growth occur in photolysis. Figure 3d and e show the density of bracelet-shaped nanostructures on the graphene surface consisting of five or six Cr_xO_3 NPs that are around 100 nm in diameter. This bracelet-like arrangement of Cr_xO_3 NPs on the graphene surface (25 °C) is attributed to magnetic moment-directed self-assembly.[55] Cr_2O_3 NPs are antiferromagnetic, with the presence of a net magnetic moment at its surface, corresponding to imbalanced spin numbers below the Néel temperature.[56] Therefore, it is speculated that the magnetic

moments are induced in the mixture of antiferromagnetic Cr_xO_3 nanoparticles, in which internal structural defects and surface spins are unbalanced.[57,58] As a result, the formation of the bracelet-shaped NPs can be directed by the magnetic moments of Cr_xO_3 NPs, while the dipolar interactions compete with nondirectional van der Waals interactions at short range.[59] Further, the bracelet-shaped NPs are not observed at 50 °C, consistent with the disappearance of magnetic moments when the temperature exceeds the Néel temperature ($T_N = 308$ K for the bulk Cr_2O_3 and decreases with reducing the particle size).[60] To confirm the attachment of TMONs on graphene and comprehend its binding mechanism, XPS (Kratos AXIS-165) characterization was performed. In Figure 3f, the core level Cr 2p-peaks under high-resolution scan (dotted line) is fitted by the Lorentzian−Gaussian equation (solid line). The Cr peaks centered at 576.55 eV ($2p_{3/2}$) and 586.38 eV ($2p_{1/2}$) are assigned to Cr(III),[61] while the peaks at higher binding energy (578.75 eV for $2p_{3/2}$ and 588.35 for $2p_{1/2}$) correspond to Cr(VI).[62] This indicates that the chromium oxide nanoparticles are formed as a mixture of Cr_2O_3 and CrO_3. Further, the energy dispersive spectroscopy (EDS) analysis in Figure S5 shows the chromium adsorption peaks located in the range of 0−1 keV and 5−6 keV,[63] confirming the presence of Cr_xO_3 nanoparticles on the graphene surface. In addition to temperature, the effects of irradiation time and light source on nanoparticles' morphology are also investigated. In Figure S6, it is observed that the density of NPs incorporated on the graphene surface is increased quickly between 1 and 3 h and then slowly between 3 and 5 h. Since the η^6-functionalization acts as active sites for the attachment of NPs on the graphene surface and the formation energy of (η^6-benzene)$Cr(CO)_3$ (Δ_fH(benzene-$Cr(CO)_3 = -341.6$ kJ/mol[64]) is larger than the dissociation energy of Cr-CO (D(Cr−CO)= −35.8 kJ/mol),[65] it indicates that during 1−3 h the rate of the η^6 reaction limits the density of NPs attached on the graphene sheets. Moreover, during 3−5 h a large quantity of nanoparticles grows larger (see Figure S6e and f). UVC light (wavelength $\lambda = 200−280$ nm) offers higher energy than LED white light, so that both the size and density
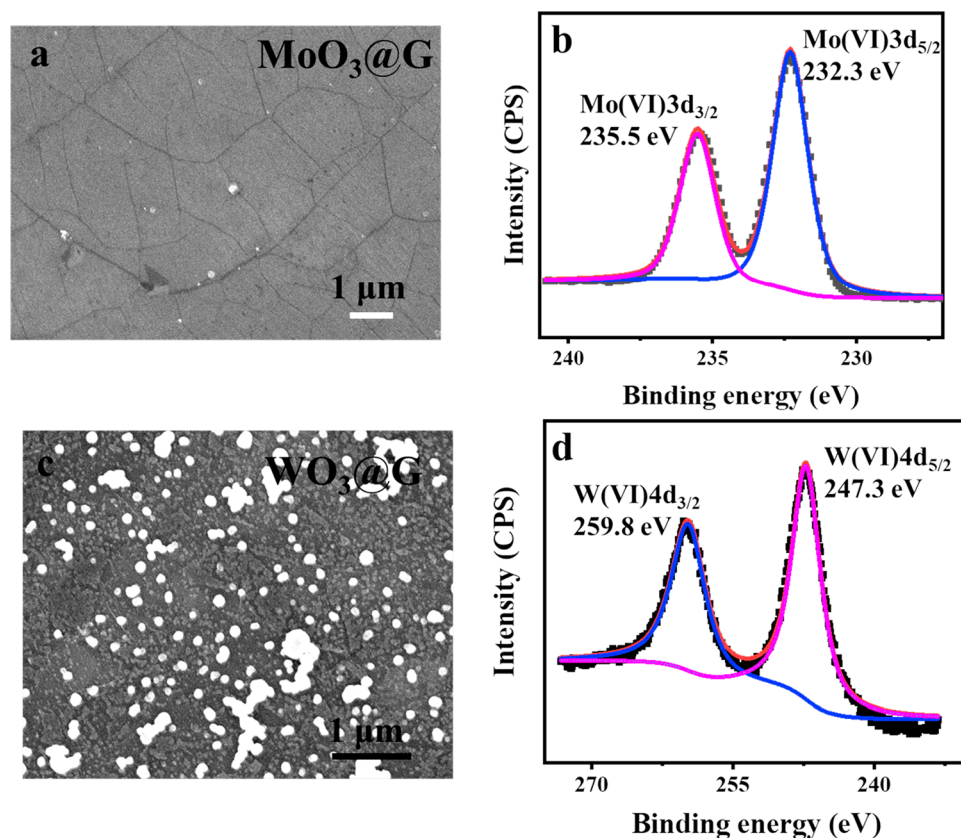
Figure 4. FESEM and XPS characterization of MoO₃- and WO₃NPs-decorated graphene: FESEM topography images of (a) MoO₃NPs@G and (c) WO₃NPs@G. High-resolution XPS spectra of (b) Mo 3d-peaks and (d) W 4d-peaks.
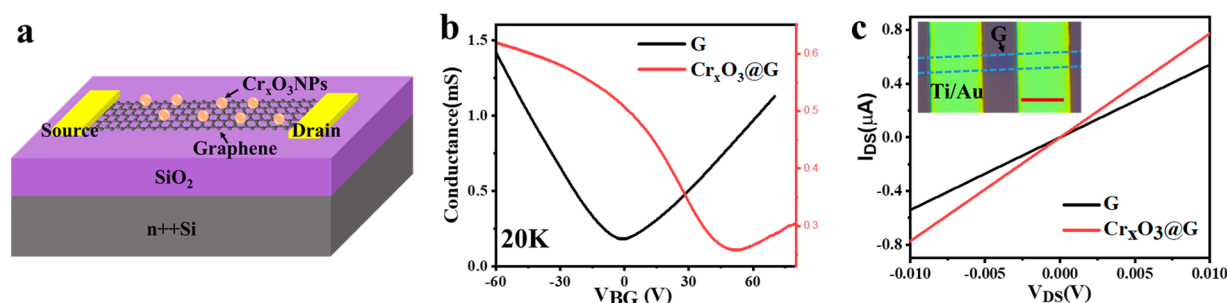

Figure 5. Electronic transport measurements of graphene field-effect transistor (FET) devices: (a) Schematic of a graphene back-gated FET device with Ti/Au as electrode contacts. (b) Profiles of conductance *versus* back-gate voltage (V_{BG}) of pristine graphene (black line) and Cr_xO_3 NPs-decorated graphene (red line) at T = 20 K with V_{DS} = 10 mV. (c) I_{DS} *versus* V_{DS} (source−drain voltage) at T = 20 K obtained on graphene devices before and after incorporation of Cr_xO_3 NPs. The inset shows an optical image of the graphene channel used for electrical studies (scale bar = 10 μm).

of NPs are higher than those under LED white light (see Figure S7). In order to control the size of NPs more conveniently, LED white light is used in this work.

The nanostructured composites of MoO₃ and WO₃ combined with other materials (*e.g.*, rGO, carbon nanotube, and silicon) have been widely used in the application areas of gas sensing,[13,20] batteries,[66] supercapacitors,[67] photocatalysis,[68] and the environment.[69] Therefore, by using analogous reactants under the same conditions, we attached MoO₃ and WO₃ nanoparticles on graphene. As shown in Figure 4a and c, the density of the TMONs on graphene generally follows WO₃ > Cr$_x$O₃ > MoO₃ NPs. Like Cr$_x$O₃ NPs, the attachments of MoO₃ and WO₃ were also confirmed by XPS. In Figure 4b, the Mo 3d-peaks are fitted by using the Lorentzian−Gaussian

equation and observed at 235.5 eV (3d$_{3/2}$) and 232.3 eV (3d$_{5/2}$), assigned to Mo(VI).[70,71] The W(VI) 4d$_{3/2}$ and W(VI) 4d$_{5/2}$ peaks are located at 259.8 and 247.3 eV,[72] respectively, as shown in Figure 4d. The C 1s peak (Figure S4) is deconvoluted into three components in both pristine graphene and TMONs@graphene, including sp^2 C−C (284.2 eV),[62] C−O (285.6 eV), and C≡O (288.0 ± 0.1 eV). The C−O peak is attributed to the poly(methyl methacrylate) (PMMA) residue from the transfer process or adventitious carbon.[73,74] The C≡O peak corresponds to TM(CO)₃ groups, so it is not observed in pristine graphene. This further proves that the η^6-chemistry occurs on graphene's basal surface, which acts as an active site for TMON nucleation and attachment. Moreover, the Raman
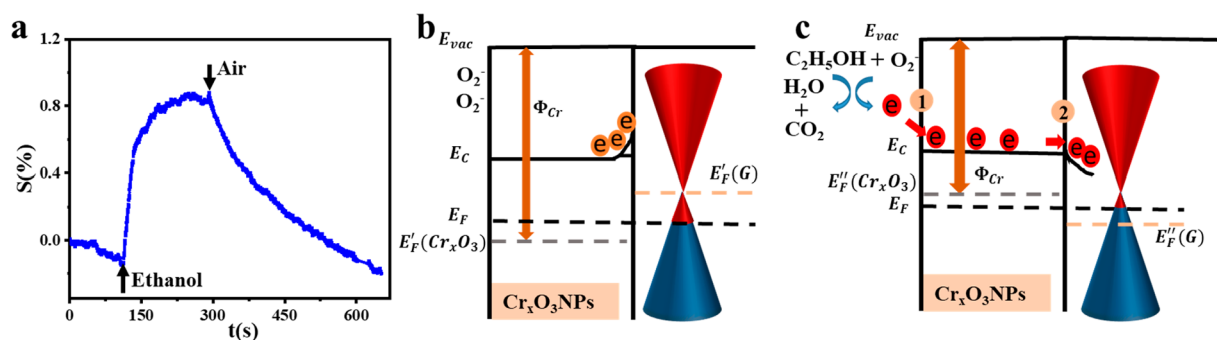
Figure 6. Molecular sensing of TMON-incorporated η^6-graphene: (a) Ethanol gas absorption behavior of $Cr_xO_3@G$ devices at room temperature (300 K). (b) Electronic band diagram of $Cr_xO_3@G$ by absorbing O_2 on the surface. $E'_F(Cr_xO_3)$ and $E'_F(G)$ are Fermi level of Cr_xO_3 and graphene before interfacing with each other, respectively. (c) Schematic diagram of proposed cascaded-doping mechanism while $Cr_xO_3@G$ are exposed to ethanol. $E''_F(Cr_xO_3)$ represents the Fermi level of Cr_xO_3 after exposure to ethanol. $E''_F(G)$ is the Fermi level of doped graphene by Cr_xO_3 NPs. Φ_{Cr} represents the work function of Cr_xO_3. Interface 1 is the surface when ethanol is attached on the Cr_xO_3 NP surface. Interface 2 is formed when Cr_xO_3 NPs are attached on graphene.

spectra in Figures S9 and S10 show that blue shifts of G- and 2D-bands resulting in $MoO_3NPs@G$ and $WO_3NPs@G$.

In order to investigate the influence of Cr_xO_3 NPs on graphene's electrical properties, the charge-carrier transport characterization was performed on graphene back-gated field-effect transistor (FET) devices. After graphene sheets were transferred onto 300 nm SiO_2-coated Si substrates, the devices were fabricated by metallization and photolithography process steps. Figure 5a is a schematic diagram of the back-gated graphene FET device, with Ti/Au (10 nm/60 nm) as contact electrodes and a graphene channel of 5 μm × 3 μm (length × width) (inset of Figure 5c) (device fabrication details are outlined in the Materials and Methods section). Figure 5b displays a plot of conductance as a function of back-gate voltage (V_{BG}) at 20 K. After the incorporation of Cr_xO_3 NPs on graphene, the Dirac voltage (V_D) shifts to 50 V from 0 V, which indicates heavy p-doping of graphene with Cr_xO_3 NPs and also a change in the Fermi level. The Fermi level can be tuned by the interfacial interactions between the metal oxide nanoparticles and graphene and/or by a different work function of NPs.[75,76] As mentioned earlier, the work function of graphene is relatively smaller than that of Cr_xO_3 NPs. This will lead to electron transfer from graphene to NPs, causing the Fermi energy to reduce by 250 meV following the equation $E_F(n) = \hbar|v_F|\sqrt{\pi n}$,[49] where $|v_F|$ is the Fermi velocity ($|v_F| = 1.1 \times 10^6$ ms^{-1}) and n is the carrier density induced by incorporation of NPs (estimated to be 3.78×10^{12} cm^{-2} from the equation[77] $n = \frac{C_o(V_{D,CrxO3NPs} - V_{D,G})}{e}$, where C_o is the dielectric capacitance, $V_{D,CrxO3NPs}$ is the Dirac point of Cr_xO_3NPs-decorated graphene, $V_{D,G}$ is the Dirac point of pristine graphene, and e is the electron charge). Further, the field effect mobility (μ_{FET}) is calculated using the Drude formula[78] $\mu_{FET} = \left(\frac{1}{C_0}\right)\left(\frac{d\sigma}{dV_{BG}}\right)\left(\frac{L}{W}\right)$, where σ is the conductance, V_{BG} is the back-gating voltage, and L and W are the length and width of the graphene channel, respectively. μ_{FET}(hole) are estimated to be 2220 and 115 cm^2 V^{-1} s^{-1} for graphene and $Cr_xO_3@G$ devices, respectively. Since the attachment of Cr_xO_3 NPs on graphene will introduce potential barriers causing short-range and long-range scattering sites, the carrier mobility is reduced by an order of magnitude.[79]

The transition metal oxide nanostructures are widely used to combine with carbon materials (*e.g.*, carbon nanotubes

(CNTs), rGO) to improve the gas-sensing performance. For these nanohybrid material systems, electron transfer occurs at the interface of transition metal oxide nanostructures and carbon materials. Moreover, while the nanohybrids are exposed to gas molecules, the formed cascaded-based doping will alter both the Fermi level and resistivity of carbon materials. Lu *et al.*[80] coated CNTs with tin oxide (SnO_2) nanocrystals to detect NO_2, CO, and H_2. They proposed that the CNT's Fermi level shifted toward the valence band and the conductivity was enhanced correspondingly when exposed to NO_2 gas, due to the cascaded-electron transfer from CNT toward SnO_2 at the interface and then toward absorbed NO_2 molecules. Wang and co-workers[81] find when the prepared WO_3 nanorods/sulfonated rGO (S-rGO) nanocomposites interface with NO_2 molecules, NO_2's continuous electron capture at the surface of WO_3 shifts the Fermi level of WO_3 lower than that in S-rGO, so that electrons transfer from S-rGO to WO_3, leading to enhanced conductivity of WO_3/S-rGO nanocomposites. Here, by leveraging the affinity of Cr_xO_3 NPs to ethanol, an ethanol-detection device construct was tested by measuring the resistance with changing ethanol concentration around the sensor chip. The ethanol gas flow is introduced by connecting a bubbler system, where nitrogen gas (with a purity of 99.9%) acts as a carrier. To investigate the reproducibility of $Cr_xO_3@G$ devices at room temperature, the ethanol vapor mixed with N_2 (1000 sccm) is switched on and off (exposed to air) at variable time intervals. The sensing response (S) is calculated as $S = \frac{R_e - R_0}{R_0} \times 100\%$, where R_e represents the resistance in the presence of ethanol vapor and R_0 is the resistance when exposed to air. Figure 6a indicates that the resistance is enhanced resulting from the absorption of ethanol molecules on the $Cr_xO_3@G$ surface, while the resistance is recovered as ethanol vapor is replaced by air.

A cascaded-doping mechanism involving transfer of electrons from ethanol to graphene through Cr_xO_3 NPs (Figure 6c) is proposed for the increased resistance. First, p-doped graphene is formed postattachment of Cr_xO_3 NPs, in which electrons transfer to high-work-function Cr_xO_3 NPs from graphene. When the p-type $Cr_xO_3@G$ devices are exposed to air, the adsorbed oxygen molecules take electrons near their surface to form ionic species O_2^- at room temperature,[82] as shown in eq 3 and Figure 6b. Second, the cascaded-electron transfer is carried out when $Cr_xO_3@G$

devices interface with ethanol. The adsorbed (reducing) ethanol molecules on the Cr_xO_3 surface catalytically react with O_2^- (also adsorbed) to form H_2O and CO_2, releasing electrons to Cr_xO_3[83,84] (interface 1), shown in eq 4. After accepting electrons, Cr_xO_3's Fermi level is moved upward, which is even higher than that of graphene ($E_F''(Cr_xO_3) > E_F''(G)$), shown in Figure 6c). As a result, the difference of Fermi levels pushes electrons into graphene from Cr_xO_3 (interface 2). The electron addition into the valence band reduces the density of the majority charge carrier (holes) in graphene, resulting in an upshift of graphene's Fermi level and an increase in its resistivity. The mechanism involves electron transfer from ethanol to graphene through two interfaces and is therefore denoted as cascaded doping. Consistently, it is shown in Figure S11 that the absorbance of ethanol on pristine graphene results in reduced resistance due to ethanol's donor characteristics.

$$O_2(gas) + e^- \leftrightharpoons O_2^-(ads) \tag{3}$$

$$C_2H_5OH + 3O_2^-(ads) \rightarrow 3H_2O + 2CO_2 + 3e^- \tag{4}$$
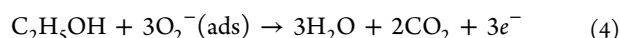
CONCLUSIONS

A unique photo-organometallic route is reported to anchor transition metal oxide nanoparticles (Cr_xO_3, WO_3, and MoO_3) of 50−100 nm radius on graphene without distorting graphene's sp^2-hybridization. The thermal energy plays a vital role in controlling the deposition density and morphology of nanoparticles on graphene's surface. Further, room-temperature, magnetic-moment-directed self-assembly of Cr_xO_3 nanoparticles into a bracelet structure on graphene was also achieved. The XPS high-resolution spectroscopy confirms that there are two valence phases of chromium (III and VI) formed in Cr_xO_3 nanoparticles and one (VI) in MoO_3 and WO_3 nanoparticles. Low-temperature electronic transport measurements on FET devices of Cr_xO_3 nanoparticles deposited on graphene show p-doping (hole density = 3.78×10^{12} cm^{-2}) with 250 mV lower Fermi level, which is also consistent with a blue shift in both G and 2D Raman vibrational bands. The electrical conductivity is enhanced due to the increase of carriers, while the mobility is reduced, resulting from the scattering effect of nanoparticle-interfaced graphene. The absorption of ethanol gas on the surface of Cr_xO_3 NPs incorporated graphene enhances the resistance via the proposed cascaded-doping mechanism, while it results in a decrease of resistance on pristine graphene devices.

MATERIALS AND METHODS

TMONs Attachment. Transferred CVD graphene on a 300 nm SiO_2/Si chip is exposed to 15 mL of 50 mM transition metal hexacarbonyl ($TM(CO)_6$, TM = Mo, Cr, and W)/THF/dibutyl ether solution (THF:dibutyl ether = 1:2). THF is used to dissolve the sublimated solid. By connecting to a vacuum pump and with LED white light (wavelength λ = 450−475 nm) irradiating on the solution, the reaction occurs under vacuum. After 3 h, the chip is washed with acetone and isopropyl alcohol (IPA) to remove those unattached nanoparticles, followed by being dried with N_2 gas. A schematic of the experimental setup is shown in Figure 1a.

Raman Spectroscopy and Mapping. The confocal Raman microscope (Raman-AFM, WITec alpha 300 RA, laser wavelength of 532 nm) is used to obtain the Raman spectroscopy and spatial Raman mapping. The laser spot size is 721 nm by using a 100× objective lens (numerical aperture = 0.90). All the Raman maps had a pixel size of 0.08 μm for both x- and y-directions. Before and after the attachments

of Cr_xO_3 NPs, the transferred graphene on SiO_2/Si with a region of 4 × 4 μm^2 was scanned to obtain the G-peak (from 1581 to 1592 cm^{-1}) and 2D-band (from 2670 to 2682 cm^{-1}) position mappings and the intensity ratio between the D-band and G-band (I_D/I_G).

Device Fabrication and Electronic Transport Measurements. The electrical contacts (Ti/Au, 10 nm/60 nm) were deposited on transferred graphene chips via electron beam evaporation (Temescal FC2000). The LOR 3A was spin-coated onto a sample at 3000 rpm for 35 s, followed by hard baking at 175 °C for 5 min. Then the positive photoresist (1811) was deposited onto the samples at 3000 rpm for 35 s. The samples were baked on the hot plate at 115 °C for 1 min. Photolithography (Laser Pattern Generator, Microtech LW405) was used to define contact pattern. The graphene channel with a length of 5 μm and width of 3 μm (as shown in Figure 5c) was obtained via oxygen reactive ion etching (RIE, Oxford) to remove the unwanted graphene. Subsequently, the photoresists were removed by exposing the samples to 1165 remover. After annealing under vacuum at 200 °C to remove residuals, the back-gated graphene transistors were measured with a source meter (Keithley 2612) in a variable-temperature probe station (ARS cryostat). The measurements are performed under vacuum (∼10^{-3} Pa).

ASSOCIATED CONTENT

Ⓢ Supporting Information

The Supporting Information is available free of charge on the ACS Publications website at DOI: 10.1021/acsnano.9b05484.

> Raman mapping of D-band intensity, AFM and Raman characterization on MoO_3-deposited graphene, FESEM image of pristine graphene, XPS of carbon 1s peaks in graphene and TMONs@G, EDS of Cr_xO_3 NPs deposited on graphene, FESEM images of Cr_xO_3 NPs deposited on graphene at 50 °C for variable irradiation time, FESEM images of Cr_xO_3 NPs deposited on graphene at 25 °C using UVC light and LED white light, FESEM images of Cr_xO_3 NPs deposited on graphene for annealing test, Raman characterization of MoO_3 deposited on graphene, Raman characterization of WO_3 deposited on graphene, ethanol-sensing effect of pristine graphene (PDF)

AUTHOR INFORMATION

Corresponding Author
*E-mail: vikasb@uic.edu.

ORCID 🄳
Sanjay K. Behura: 0000-0001-7339-9997
Vikas Berry: 0000-0002-1102-1996

Notes
The authors declare no competing financial interest.

REFERENCES

(1) Bonaccorso, F.; Colombo, L.; Yu, G.; Stoller, M.; Tozzini, V.; Ferrari, A. C.; Ruoff, R. S.; Pellegrini, V. Graphene, Related Two-Dimensional Crystals, and Hybrid Systems for Energy Conversion

and Storage. *Science (Washington, DC, U. S.)* **2015**, *347*, 1246501−1246501.

(2) Raccichini, R.; Varzi, A.; Passerini, S.; Scrosati, B. The Role of Graphene for Electrochemical Energy Storage. *Nat. Mater.* **2015**, *14*, 271−279.

(3) Schwierz, F. Graphene Transistors. *Nat. Nanotechnol.* **2010**, *5*, 487−496.

(4) Zhang, Y.; Liu, S.; Wang, L.; Qin, X.; Tian, J.; Lu, W.; Chang, G.; Sun, X. One-Pot Green Synthesis of Ag Nanoparticles-Graphene Nanocomposites and Their Applications in SERS, H_2O_2, and Glucose Sensing. *RSC Adv.* **2012**, *2*, 538−545.

(5) Lu, C. H.; Yang, H. H.; Zhu, C. L.; Chen, X.; Chen, G. N. A Graphene Platform for Sensing Biomolecules. *Angew. Chem., Int. Ed.* **2009**, *48*, 4785−4787.

(6) Satoh, N.; Nakashima, T.; Kamikura, K.; Yamamoto, K. Quantum Size Effect in TiO_2 Nanoparticles Prepared by Finely Controlled Metal Assembly on Dendrimer Templates. *Nat. Nanotechnol.* **2008**, *3*, 106−111.

(7) Han, Y.; Rheem, Y.; Lee, K.-H.; Kim, H.; Myung, N. V. Synthesis and Characterization of Orthorhombic-MoO_3 Nanofibers with Controlled Morphology and Diameter. *J. Ind. Eng. Chem.* **2018**, *62*, 231−238.

(8) Ghosh, M.; Biswas, K.; Sundaresan, A.; Rao, C. N. R. MnO and NiO Nanoparticles: Synthesis and Magnetic Properties. *J. Mater. Chem.* **2006**, *16*, 106−111.

(9) Zhao, Y.; Li, C.; Liu, X.; Gu, F.; Jiang, H.; Shao, W.; Zhang, L.; He, Y. Synthesis and Optical Properties of TiO_2 Nanoparticles. *Mater. Lett.* **2007**, *61*, 79−83.

(10) Franke, M. E.; Koplin, T. J.; Simon, U. Metal and Metal Oxide Nanoparticles in Chemiresistors: Does the Nanoscale Matter? *Small* **2006**, *2*, 36−50.

(11) Shendage, S. S.; Patil, V. L.; Vanalakar, S. A.; Patil, S. P.; Harale, N. S.; Bhosale, J. L.; Kim, J. H.; Patil, P. S. Sensitive and Selective NO_2 Gas Sensor Based on WO_3 Nanoplates. *Sens. Actuators, B* **2017**, *240*, 426−433.

(12) Cai, Z.-X.; Li, H.-Y.; Yang, X.-N.; Guo, X. NO Sensing by Single Crystalline WO_3 Nanowires. *Sens. Actuators, B* **2015**, *219*, 346−353.

(13) Liu, Y.; Huang, J.; Gong, Y.; Xu, X.; Li, H. Liquid Flame Spray Fabrication of WO_3 -Reduced Graphene Oxide Nanocomposites for Enhanced O_3 -Sensing Performances. *Ceram. Int.* **2017**, *43*, 13185−13192.

(14) Zhang, L.; Liu, Z.; Jin, L.; Zhang, B.; Zhang, H.; Zhu, M.; Yang, W. Self-Assembly Gridding α-MoO_3 Nanobelts for Highly Toxic H2S Gas Sensors. *Sens. Actuators, B* **2016**, *237*, 350−357.

(15) Lu, N.; Gao, X.; Yang, C.; Xiao, F.; Wang, J.; Su, X. Enhanced Formic Acid Gas-Sensing Property of WO_3 Nanorod Bundles *via* Hydrothermal Method. *Sens. Actuators, B* **2016**, *223*, 743−749.

(16) Xiao, T.; Wang, X.-Y.; Zhao, Z.-H.; Li, L.; Zhang, L.; Yao, H.-C.; Wang, J.-S.; Li, Z.-J. Highly Sensitive and Selective Acetone Sensor Based on C-Doped WO_3 for Potential Diagnosis of Diabetes Mellitus. *Sens. Actuators, B* **2014**, *199*, 210−219.

(17) Ahmed, B.; Shahid, M.; Nagaraju, D. H.; Anjum, D. H.; Hedhili, M. N.; Alshareef, H. N. Surface Passivation of MoO_3 Nanorods by Atomic Layer Deposition toward High Rate Durable Li Ion Battery Anodes. *ACS Appl. Mater. Interfaces* **2015**, *7*, 13154−13163.

(18) Wang, W.; Qin, J.; Yin, Z.; Cao, M. Achieving Fully Reversible Conversion in MoO_3 for Lithium Ion Batteries by Rational Introduction of $CoMoO_4$. *ACS Nano* **2016**, *10*, 10106−10116.

(19) Mendoza-Sánchez, B.; Hanlon, D.; Coelho, J.; Brien, S. O.; Pettersson, H.; Coleman, J.; Nicolosi, V. An Investigation of the Energy Storage Properties of a 2D α-MoO_3 -SWCNTs Composite Films. *2D Mater.* **2017**, *4*, No. 015005.

(20) MalekAlaie, M.; Jahangiri, M.; Rashidi, A. M.; HaghighiAsl, A.; Izadi, N. Selective Hydrogen Sulfide (H_2S) Sensors Based on Molybdenum Trioxide (MoO_3) Nanoparticle Decorated Reduced Graphene Oxide. *Mater. Sci. Semicond. Process.* **2015**, *38*, 93−100.

(21) Lei, S.; Peng, X.; Liang, Z.; Li, X.; Wang, C.; Cheng, B.; Xiao, Y.; Zhou, L. Self-Template Formation and Properties Study of Cr_2O_3 Nanoparticle Tubes. *J. Mater. Chem.* **2012**, *22*, 1643−1651.

(22) Rajagopal, S.; Bharaneswari, M.; Nataraj, D.; Khyzhun, O. Y.; Djaoued, Y. Crystal Structure and Electronic Properties of Facile Synthesized Cr_2O_3 Nanoparticles. *Mater. Res. Express* **2016**, *3*, No. 095019.

(23) Jankovský, O.; Sedmidubský, D.; Sofer, Z.; Luxa, J.; Bartůněk, V. Simple Synthesis of Cr_2O_3 Nanoparticles with a Tunable Particle Size. *Ceram. Int.* **2015**, *41*, 4644−4650.

(24) Craciun, M. F.; Khrapach, I.; Barnes, M. D.; Russo, S. Properties and Applications of Chemically Functionalized Graphene. *J. Phys.: Condens. Matter* **2013**, *25*, 423201.

(25) Liang, D.; Cui, C.; Hu, H.; Wang, Y.; Xu, S.; Ying, B.; Li, P.; Lu, B.; Shen, H. One-Step Hydrothermal Synthesis of Anatase TiO_2/Reduced Graphene Oxide Nanocomposites with Enhanced Photocatalytic Activity. *J. Alloys Compd.* **2014**, *582*, 236−240.

(26) Chu, X.; Hu, T.; Gao, F.; Dong, Y.; Sun, W.; Bai, L. Gas Sensing Properties of Graphene−WO_3 Composites Prepared by Hydrothermal Method. *Mater. Sci. Eng., B* **2015**, *193*, 97−104.

(27) Wang, B.; Su, D.; Park, J.; Ahn, H.; Wang, G. Graphene-Supported SnO_2 Nanoparticles Prepared by a Solvothermal Approach for an Enhanced Electrochemical Performance in Lithium-Ion Batteries. *Nanoscale Res. Lett.* **2012**, *7*, 215.

(28) Zhang, X.; Sun, X.; Chen, Y.; Zhang, D.; Ma, Y. One-Step Solvothermal Synthesis of Graphene/Mn_3O_4 Nanocomposites and Their Electrochemical Properties for Supercapacitors. *Mater. Lett.* **2012**, *68*, 336−339.

(29) Shu, W.; Liu, Y.; Peng, Z.; Chen, K.; Zhang, C.; Chen, W. Synthesis and Photovoltaic Performance of Reduced Graphene Oxide−TiO_2 Nanoparticles Composites by Solvothermal Method. *J. Alloys Compd.* **2013**, *563*, 229−233.

(30) Dai, J.; Zhao, Y.; Wu, X.; Zeng, X. C.; Yang, J. Organometallic Hexahapto-Functionalized Graphene: Band Gap Engineering with Minute Distortion to the Planar Structure. *J. Phys. Chem. C* **2013**, *117*, 22156−22161.

(31) Sarkar, S.; Zhang, H.; Huang, J.-W.; Wang, F.; Bekyarova, E.; Lau, C. N.; Haddon, R. C. Organometallic Hexahapto Functionalization of Single Layer Graphene as a Route to High Mobility Graphene Devices. *Adv. Mater.* **2013**, *25*, 1131−1136.

(32) Sarkar, S.; Niyogi, S.; Bekyarova, E.; Haddon, R. C. Organometallic Chemistry of Extended Periodic π-Electron Systems: Hexahapto-Chromium Complexes of Graphene and Single-Walled Carbon Nanotubes. *Chem. Sci.* **2011**, *2*, 1326.

(33) Che, S.; Jasuja, K.; Behura, S. K.; Nguyen, P.; Sreeprasad, T. S.; Berry, V. Retained Carrier-Mobility and Enhanced Plasmonic-Photovoltaics of Graphene *via* Ring-Centered η^6 Functionalization and Nanointerfacing. *Nano Lett.* **2017**, *17*, 4381−4389.

(34) Pekker, A.; Chen, M.; Bekyarova, E.; Haddon, R. C. Photochemical Generation of Bis-Hexahapto Chromium Interconnects between the Graphene Surfaces of Single-Walled Carbon Nanotubes. *Mater. Horiz.* **2015**, *2*, 81−85.

(35) Chen, M.; Tian, X.; Li, W.; Bekyarova, E.; Li, G.; Moser, M.; Haddon, R. C. Application of Organometallic Chemistry to the Electrical Interconnection of Graphene Nanoplatelets. *Chem. Mater.* **2016**, *28*, 2260−2266.

(36) Chen, M.; Pekker, A.; Li, W.; Itkis, M. E.; Haddon, R. C.; Bekyarova, E. Organometallic Chemistry of Graphene: Photochemical Complexation of Graphene with Group 6 Transition Metals. *Carbon* **2018**, *129*, 450−455.

(37) Wrighton, M. The Photochemistry of Metal Carbonyls. *Chem. Rev.* **1974**, *74*, 401−430.

(38) Kostermans, G. B. M.; Bobeldijk, M.; Kwakman, P. J.; de Wolf, W. H.; Bickelhaupt, F. Photochemical Synthesis of Arenetricarbonylchromium(0) Complexes: Scope and Limitations. *J. Organomet. Chem.* **1989**, *363*, 291−296.

(39) Ercoli, R.; Calderazzo, F. X-Ray Determination of the Structure of Tricarbonylchromium-Benzene. *Communications* **1959**, *287*, 2271−2272.

(40) Patra, M.; Merz, K.; Metzler-Nolte, N. Planar Chiral (η^6-Arene)Cr(CO)$_3$ Containing Carboxylic Acid Derivatives: Synthesis and Use in the Preparation of Organometallic Analogues of the Antibiotic Platensimycin. *Dalton Trans.* **2012**, *41*, 112−117.

(41) Zhong, Z. C.; Cheng, R. H.; Bosley, J.; Dowben, P. A.; Sellmyer, D. J. Fabrication of Chromium Oxide Nanoparticles by Laser-Induced Deposition from Solution. *Appl. Surf. Sci.* **2001**, *181*, 196−200.

(42) Krämer, J.; Redel, E.; Thomann, R.; Janiak, C. Use of Ionic Liquids for the Synthesis of Iron, Ruthenium, and Osmium Nanoparticles from Their Metal Carbonyl Precursors. *Organometallics* **2008**, *27*, 1976−1978.

(43) Redel, E.; Thomann, R.; Janiak, C. Use of Ionic Liquids (ILs) for the IL-Anion Size-Dependent Formation of Cr, Mo and W Nanoparticles from Metal Carbonyl M(CO)$_6$ Precursors. *Chem. Commun.* **2008**, *15*, 1789.

(44) Eremin, A. V.; Gurentsov, E. V. Sizing of Mo Nanoparticles Synthesised by Kr−F Laser Pulse Photo-Dissociation of Mo(CO)6. *Appl. Phys. A: Mater. Sci. Process.* **2015**, *119*, 615−622.

(45) Li, B.; Zhou, L.; Wu, D.; Peng, H.; Yan, K.; Zhou, Y.; Liu, Z. Photochemical Chlorination of Graphene. *ACS Nano* **2011**, *5*, 5957−5961.

(46) Niyogi, S.; Bekyarova, E.; Itkis, M. E.; Zhang, H.; Shepperd, K.; Hicks, J.; Sprinkle, M.; Berger, C.; Lau, C. N.; DeHeer, W. A.; Conrad, E. H. Spectroscopy of Covalently Functionalized Graphene. *Nano Lett.* **2010**, *10*, 4061−4066.

(47) Bruna, M.; Ott, A. K.; Ijäs, M.; Yoon, D.; Sassi, U.; Ferrari, A. C. Doping Dependence of the Raman Spectrum of Defected Graphene. *ACS Nano* **2014**, *8*, 7432−7441.

(48) Iqbal, M. W.; Iqbal, M. Z.; Khan, M. F.; Jin, X.; Hwang, C.; Eom, J. Modification of the Structural and Electrical Properties of Graphene Layers by Pt Adsorbates. *Sci. Technol. Adv. Mater.* **2014**, *15*, No. 055002.

(49) Das, A.; Pisana, S.; Chakraborty, B.; Piscanec, S.; Saha, S. K.; Waghmare, U. V.; Novoselov, K. S.; Krishnamurthy, H. R.; Geim, A. K.; Ferrari, A. C.; Sood, A. K. Monitoring Dopants by Raman Scattering in an Electrochemically Top-Gated Graphene Transistor. *Nat. Nanotechnol.* **2008**, *3*, 210−215.

(50) Daukiya, L.; Mattioli, C.; Aubel, D.; Hajjar-Garreau, S.; Vonau, F.; Denys, E.; Reiter, G.; Fransson, J.; Perrin, E.; Bocquet, M. L.; Bena, C. Covalent Functionalization by Cycloaddition Reactions of Pristine Defect-Free Graphene. *ACS Nano* **2017**, *11*, 627−634.

(51) Greiner, M. T.; Chai, L.; Helander, M. G.; Tang, W.-M.; Lu, Z.-H. Transition Metal Oxide Work Functions: The Influence of Cation Oxidation State and Oxygen Vacancies. *Adv. Funct. Mater.* **2012**, *22*, 4557−4568.

(52) Syed, S. R.; Lim, G.-H.; Flanders, S. J.; Taylor, A. B.; Lim, B.; Chon, J. W. M. Single Layer Graphene Band Hybridization with Silver Nanoplates: Interplay between Doping and Plasmonic Enhancement. *Appl. Phys. Lett.* **2016**, *109*, 103103.

(53) Giovannetti, G.; Khomyakov, P. A.; Brocks, G.; Karpan, V. M.; van den Brink, J.; Kelly, P. J. Doping Graphene with Metal Contacts. *Phys. Rev. Lett.* **2008**, *101*, No. 026803.

(54) Shi, X.; Dong, G.; Fang, M.; Wang, F.; Lin, H.; Yen, W.-C.; Chan, K. S.; Chueh, Y.-L.; Ho, J. C. Selective *N*-Type Doping in Graphene *via* the Aluminium Nanoparticle Decoration Approach. *J. Mater. Chem. C* **2014**, *2*, 5417−5421.

(55) Tripp, S. L.; Dunin-Borkowski, R. E.; Wei, A. Flux Closure in Self-Assembled Cobalt Nanoparticle Rings. *Angew. Chem., Int. Ed.* **2003**, *42*, 5591−5593.

(56) Banobre-Lopez, M.; Vazquez-Vazquez, Ca.; Rivas, J.; Lopez-Quintela, M. A. Magnetic Properties of Chromium (III) Oxide Nanoparticles. *Nanotechnology* **2003**, *14*, 318−322.

(57) Zhang, L.; Xue, D.; Gao, C. Anomalous Magnetic Properties of Antiferromagnetic CoO Nanoparticles. *J. Magn. Magn. Mater.* **2003**, *267*, 111−114.

(58) Makhlouf, S. A. Magnetic Properties of Co$_3$O$_4$ Nanoparticles. *J. Magn. Magn. Mater.* **2002**, *246*, 184−190.

(59) Tripp, S. L.; Pusztay, S. V.; Ribbe, A. E.; Wei, A. Self-Assembly of Cobalt Nanoparticle Rings. *J. Am. Chem. Soc.* **2002**, *124*, 7914−7915.

(60) Tobia, D.; Winkler, E.; Zysler, R. D.; Granada, M.; Troiani, H. E. Size Dependence of the Magnetic Properties of Antiferromagnetic Cr$_2$O$_3$ Nanoparticles. *Phys. Rev. B: Condens. Matter Mater. Phys.* **2008**, *78*, 104412.

(61) Balouria, V.; Kumar, A.; Singh, A.; Samanta, S.; Debnath, A. K.; Mahajan, A.; Bedi, R. K.; Aswal, D. K.; Gupta, S. K.; Yakhmi, J. V. Temperature Dependent H2S and Cl2 Sensing Selectivity of Cr$_2$O$_3$ Thin Films. *Sens. Actuators, B* **2011**, *157*, 466−472.

(62) Shang, M.; Liu, Y.; Liu, S.; Zeng, G.; Tan, X.; Jiang, L.; Huang, X.; Ding, Y.; Guo, Y.; Wang, S. A Novel Graphene Oxide Coated Biochar Composite: Synthesis, Characterization and Application for Cr(vi) Removal. *RSC Adv.* **2016**, *6*, 85202−85212.

(63) Santhana Krishna Kumar, A.; Ramachandran, R.; Kalidhasan, S.; Rajesh, V.; Rajesh, N. Potential Application of Dodecylamine Modified Sodium Montmorillonite as an Effective Adsorbent for Hexavalent Chromium. *Chem. Eng. J.* **2012**, *211−212*, 396−405.

(64) Li, Y.; McGrady, J. E.; Baer, T. Metal−Benzene and Metal−CO Bond Energies in Neutral and Ionic C$_6$H$_6$Cr(CO)$_3$ Studied by Threshold Photoelectron−Photoion Coincidence Spectroscopy and Density Functional Theory. *J. Am. Chem. Soc.* **2002**, *124*, 4487−4494.

(65) Lewis, K. E.; Golden, D. M.; Smith, G. P. Organometallic Bond Dissociation Energies: Laser Pyrolysis of Iron Pentacarbonyl, Chromium Hexacarbonyl, Molybdenum Hexacarbonyl, and Tungsten Hexacarbonyl. *J. Am. Chem. Soc.* **1984**, *106*, 3905−3912.

(66) Park, G. D.; Kim, J. H.; Choi, Y. J.; Kang, Y. C. Large-Scale Production of MoO$_3$-Reduced Graphene Oxide Powders with Superior Lithium Storage Properties by Spray-Drying Process. *Electrochim. Acta* **2015**, *173*, 581−587.

(67) Cao, X.; Zheng, B.; Shi, W.; Yang, J.; Fan, Z.; Luo, Z.; Rui, X.; Chen, B.; Yan, Q.; Zhang, H. Reduced Graphene Oxide-Wrapped MoO 3 Composites Prepared by Using Metal-Organic Frameworks as Precursor for All-Solid-State Flexible Supercapacitors. *Adv. Mater.* **2015**, *27*, 4695−4701.

(68) Prabhu, S.; Manikumar, S.; Cindrella, L.; Kwon, O. J. Charge Transfer and Intrinsic Electronic Properties of RGO-WO$_3$ Nanostructures for Efficient Photoelectrochemical and Photocatalytic Applications. *Mater. Sci. Semicond. Process.* **2018**, *74*, 136−146.

(69) Mu, W.; Yu, Q.; Hu, R.; Li, X.; Wei, H.; Jian, Y. Porous Three-Dimensional Reduced Graphene Oxide Merged with WO$_3$ for Efficient Removal of Radioactive Strontium. *Appl. Surf. Sci.* **2017**, *423*, 1203−1211.

(70) Chen, M.; Liu, J.; Zhou, W.; Lin, J.; Shen, Z. Nitrogen-Doped Graphene-Supported Transition-Metals Carbide Electrocatalysts for Oxygen Reduction Reaction. *Sci. Rep.* **2015**, *5*, 1−10.

(71) Zhu, Y.; Yuan, Z.; Cui, W.; Wu, Z.; Sun, Q.; Wang, S.; Kang, Z.; Sun, B. A Cost-Effective Commercial Soluble Oxide Cluster for Highly Efficient and Stable Organic Solar Cells. *J. Mater. Chem. A* **2014**, *2*, 1436−1442.

(72) Cai, Y.; Wang, Y.; Deng, S.; Chen, G.; Li, Q.; Han, B.; Han, R.; Wang, Y. Graphene Nanosheets-Tungsten Oxides Composite for Supercapacitor Electrode. *Ceram. Int.* **2014**, *40*, 4109−4116.

(73) Lin, Y. C.; Lin, C. Y.; Chiu, P. W. Controllable Graphene *N*-Doping with Ammonia Plasma. *Appl. Phys. Lett.* **2010**, *96*, 133110.

(74) Pirkle, A.; Chan, J.; Venugopal, A.; Hinojos, D.; Magnuson, C. W.; McDonnell, S.; Colombo, L.; Vogel, E. M.; Ruoff, R. S.; Wallace, R. M. The Effect of Chemical Residues on the Physical and Electrical Properties of Chemical Vapor Deposited Graphene Transferred to SiO$_2$. *Appl. Phys. Lett.* **2011**, *99*, 122108.

(75) Wu, Y.; Jiang, W.; Ren, Y.; Cai, W.; Lee, W. H.; Li, H.; Piner, R. D.; Pope, C. W.; Hao, Y.; Ji, H.; Kang, J. Tuning the Doping Type and Level of Graphene with Different Gold Configurations. *Small* **2012**, *8*, 3129−3136.

(76) Giovannetti, G.; Khomyakov, P. A.; Brocks, G.; Karpan, V. M.; van den Brink, J.; Kelly, P. J. Doping Graphene with Metal Contacts. *Phys. Rev. Lett.* **2008**, *101*, No. 026803.

(77) Ren, Y.; Chen, S.; Cai, W.; Zhu, Y.; Zhu, C.; Ruoff, R. S. Controlling the Electrical Transport Properties of Graphene by *In Situ* Metal Deposition. *Appl. Phys. Lett.* **2010**, *97*, No. 053107.

(78) Behura, S.; Nguyen, P.; Debbarma, R.; Che, S.; Seacrist, M. R.; Berry, V. Chemical Interaction-Guided, Metal-Free Growth of Large-Area Hexagonal Boron Nitride on Silicon-Based Substrates. *ACS Nano* **2017**, *11*, 4985−4994.

(79) Farmer, D. B.; Golizadeh-Mojarad, R.; Perebeinos, V.; Lin, Y.-M.; Tulevski, G. S.; Tsang, J. C.; Avouris, P. Chemical Doping and Electron−Hole Conduction Asymmetry in Graphene Devices. *Nano Lett.* **2009**, *9*, 388−392.

(80) Lu, G.; Ocola, L. E.; Chen, J. Gas Sensors: Room-Temperature Gas Sensing Based on Electron Transfer between Discrete Tin Oxide Nanocrystals and Multiwalled Carbon Nanotubes. *Adv. Mater.* **2009**, *21*, 2487−2491.

(81) Wang, T.; Hao, J.; Zheng, S.; Sun, Q.; Zhang, D.; Wang, Y. Highly Sensitive and Rapidly Responding Room-Temperature NO_2 Gas Sensors Based on WO_3 Nanorods/Sulfonated Graphene Nanocomposites. *Nano Res.* **2018**, *11*, 791−803.

(82) Kim, H.-J.; Lee, J.-H. Highly Sensitive and Selective Gas Sensors Using *P*-Type Oxide Semiconductors: Overview. *Sens. Actuators, B* **2014**, *192*, 607−627.

(83) Kamble, V. B.; Umarji, A. M. Gas Sensing Response Analysis of *P*-Type Porous Chromium Oxide Thin Films. *J. Mater. Chem. C* **2013**, *1*, 8167.

(84) Li, L.; Liu, M.; He, S.; Chen, W. Freestanding 3D Mesoporous Co_3O_4@Carbon Foam Nanostructures for Ethanol Gas Sensing. *Anal. Chem.* **2014**, *86*, 7996−8002.